

Optical attosecond pulses and tracking the nonlinear response of bound electrons

M. Th. Hassan^{1*}, T. T. Luu^{1*}, A. Moulet¹, O. Raskazovskaya², P. Zhokhov^{3,4}, M. Garg¹, N. Karpowicz¹, A. M. Zheltikov^{3,4}, V. Pervak², F. Krausz^{1,2} & E. Goulielmakis¹

The time it takes a bound electron to respond to the electromagnetic force of light sets a fundamental speed limit on the dynamic control of matter and electromagnetic signal processing. Time-integrated measurements of the nonlinear refractive index¹ of matter indicate that the nonlinear response of bound electrons to optical fields is not instantaneous; however, a complete spectral characterization of the nonlinear susceptibility tensors²—which is essential to deduce the temporal response of a medium to arbitrary driving forces using spectral measurements—has not yet been achieved. With the establishment of attosecond chronoscopy^{3–5}, the impulsive response of positive-energy electrons to electromagnetic fields has been explored through ionization of atoms⁶ and solids⁷ by an extreme-ultraviolet attosecond pulse⁸ or by strong near-infrared fields^{9–11}. However, none of the attosecond studies carried out so far have provided direct access to the nonlinear response of bound electrons. Here we demonstrate that intense optical attosecond pulses synthesized in the visible and nearby spectral ranges allow sub-femtosecond control and metrology of bound-electron dynamics. Vacuum ultraviolet spectra emanating from krypton atoms, exposed to intense waveform-controlled optical attosecond pulses, reveal a finite nonlinear response time of bound electrons of up to 115 attoseconds, which is sensitive to and controllable by the super-octave optical field. Our study could enable new spectroscopies of bound electrons in atomic, molecular or lattice potentials¹², as well as light-based electronics operating on sub-femtosecond timescales and at petahertz rates^{13–15}.

Intramolecular atomic motion dynamically distorts the interatomic electron cloud and thereby gives rise to a transient electronic polarizability¹⁶ and a finite nonlinear response of matter to light fields. Time-resolved spectroscopies can now probe this response with femtosecond lasers¹⁷. A finite nonlinear response of matter to external fields can also emerge in the absence of nuclear degrees of freedom, purely as a result of electron dynamics caused by coherent excitation of electronic states and concomitant spatiotemporal evolution of the electron cloud^{18,19}. However, quantum mechanics implies that these dynamics occur on an attosecond (as) timescale of $\Delta t \approx h/\Delta E \approx 400\text{--}800$ as (in which ΔE is the energy spacing between the relevant electronic levels, typically about 5–10 eV, and h is Planck's constant). Consequently, it has long been conjectured that the build-up of the nonlinear polarization of bound electrons under non-resonant driving by light fields is instantaneous²⁰. For electron dynamics to influence substantially the nonlinear response of a medium to an optical field and to enable its real-time tracing, both induction of electronic coherence and nonlinear probing of concomitant polarization dynamics must occur within time intervals shorter or comparable to Δt . In the visible and nearby spectral ranges, where bound electrons are typically probed and the required field strengths for nonlinear studies can be most readily produced, this condition implies a light pulse with its energy substantially being

confined to a half wave cycle. We refer to such a pulse as an optical attosecond pulse.

To illustrate how such a pulse can enable the study of the dynamics of the bound-electron response, we theoretically investigate the interaction of an intense ($4 \times 10^{13} \text{ W cm}^{-2}$) half-cycle optical field (Fig. 1a, red dashed line), identical to that used in our experiments described below, with a system lacking nuclear degrees of freedom—a krypton (Kr) atom. We calculate the induced nonlinear dipole moment $\rho(t)$ by numerical integration of the three-dimensional time-dependent Schrödinger equation (TDSE; Fig. 1a, blue line; $\rho_{\text{TDSE}}(t)$) and by using an adiabatic model describing Kr (Fig. 1a, black line; $\rho_{\text{ad}}(t)$); see Methods. The instantaneous response that is inherent to the adiabatic model is manifested by the accurate synchronization between the optical field $E(t)$ (Fig. 1a, red dashed line) and the nonlinear dipole moment $\rho_{\text{ad}}(t)$ (Fig. 1a, black line) induced in the system, and is further corroborated by the synchronous emission of the $\rho_{\text{ad}}(\omega)$ spectrum (where ω is frequency) obtained from time–frequency analysis of the dipole (Fig. 1b, left panel). In contrast, when we account for the detailed electronic structure of Kr when using the TDSE to simulate the interaction with the ultrafast optical field, coherent oscillations of the electron cloud (Fig. 1a, grey dashed line) markedly affect the nonlinear dipole $\rho_{\text{TDSE}}(t)$. The leading-edge and maximum of $\rho_{\text{TDSE}}(t)$ are noticeably retarded, relative to those of the instantaneous response $\rho_{\text{ad}}(t)$ and the driving electric field $E(t)$. The time–frequency analysis of $\rho_{\text{TDSE}}(t)$ (Fig. 1c, left panel) reveals an attosecond-scale, non-uniform retardation (group delay dispersion) of the nonlinear emission (Fig. 1c, left panel, white dashed line) that is evident across the entire dipole spectrum and extends to the resonant area (10–15 eV) of Kr. Here, the nonlinear response is dominated by long-lasting coherences that typically evolve over substantially longer timescales (Fig. 1a, grey dashed line). In contrast, the nonlinear emission at lower energies (<9 eV) is virtually confined within the time interval of the interaction of the optical field with Kr. Hence, this low-energy spectral range offers an adequate basis for exploring the dynamics of the nonlinear response of the electron cloud to the optical driver.

A comparison between the Fourier-filtered (<9 eV) nonlinear dipoles $\rho_{\text{ad}}(t)$ and $\rho_{\text{TDSE}}(t)$ predicted by the adiabatic model (Fig. 1d, black line) and the TDSE model (Fig. 1d, blue line), respectively, reveals a finite relative delay of $\tau \approx 48$ as (Fig. 1a inset). This delay represents a substantial fraction of the time span of the induced dipole $\rho_{\text{TDSE}}(t)$, which is about 250 as. The observed retardation is sensitive to, and is monotonically increasing with, applied field strength (compare the blue, orange and green lines in Fig. 1d); with an optical-field intensity of $8 \times 10^{13} \text{ W cm}^{-2}$, it reaches a value of $\tau \approx 122$ as. Figure 1e shows a similar sensitivity of the dynamics of the dipole when the field intensity is adjusted by varying the global phase ϕ_G of the driving field (justification for why the term carrier-envelope phase (CEP) is inappropriate for multi-octave waveforms is given in Methods).

¹Max-Planck-Institut für Quantenoptik, Hans-Kopfermann-Straße 1, D-85748 Garching, Germany. ²Department für Physik, Ludwig-Maximilians-Universität, Am Coulombwall 1, D-85748 Garching, Germany. ³Department of Physics and Astronomy, Texas A&M University, College Station, Texas 77843, USA. ⁴Physics Department, International Laser Center, M.V. Lomonosov Moscow State University, 119992 Moscow, Russia.

*These authors contributed equally to this work.

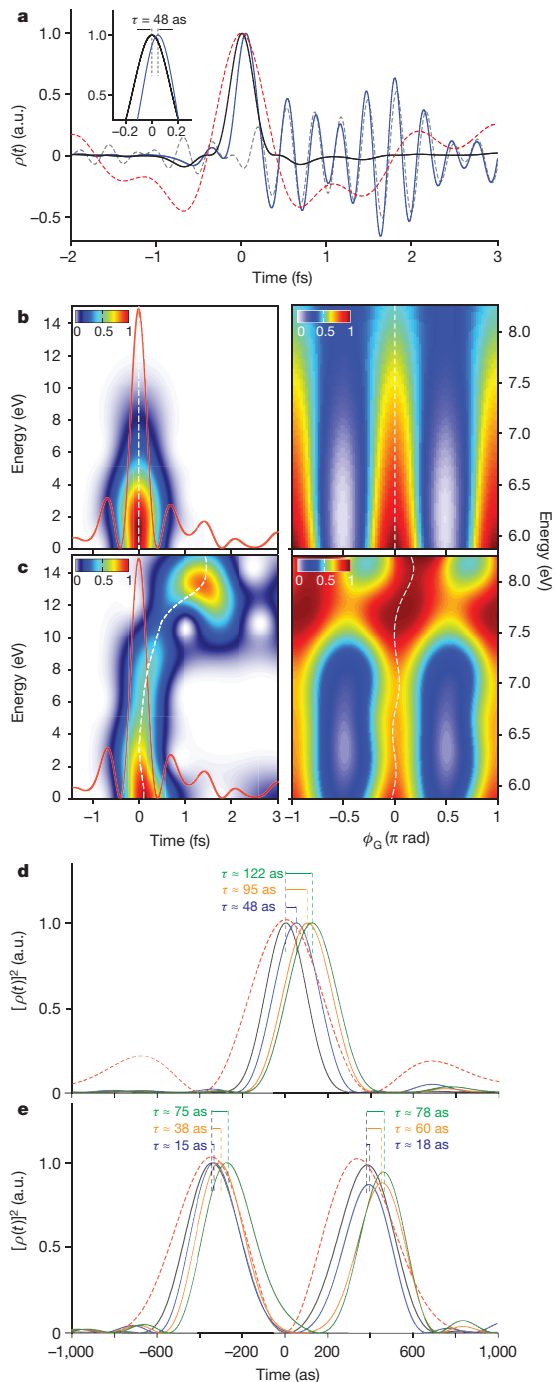


Figure 1 | Nonlinear response of bound electrons of Kr to an optical attosecond pulse. **a**, Nonlinear dipole moment $\rho(t)$ of Kr atoms subjected to an intense half-cycle optical field (dashed red line) calculated using the adiabatic ($\rho_{\text{ad}}(t)$, black line) and the TDSE ($\rho_{\text{TDSE}}(t)$, blue line) model. The dashed grey line represents the bound-electron response in the energy range (10–15 eV) that is calculated using the TDSE model. The inset shows a close-up of the peak at time $t=0$, highlighting the delay τ between the predictions of the two models. **b, c**, Time–frequency analysis of the nonlinear dipoles $\rho_{\text{ad}}(t)$ (**b**) and $\rho_{\text{TDSE}}(t)$ (**c**) (left panels); simulated nonlinear dipole spectra (5.7–8.2 eV) as a function of the global phase ϕ_G of the optical attosecond pulse predicted by the adiabatic (**b**) and TDSE (**c**) Kr models (right panels). The red line represents the instantaneous intensity of the driving field. The dashed white lines represent the centre of mass along the x axis of each plot. The colour scale represents spectral intensity in arbitrary units (a.u.). **d, e**, Low-pass-filtered (0–8 eV) normalized nonlinear dipoles for three peak intensities of the driving field: $4 \times 10^{13} \text{ W cm}^{-2}$ (blue lines), $6 \times 10^{13} \text{ W cm}^{-2}$ (orange lines) and $8 \times 10^{13} \text{ W cm}^{-2}$ (green lines) for global phases $\phi_G \approx 0$ (**d**) and $\phi_G \approx \pi/2$ rad (**e**).

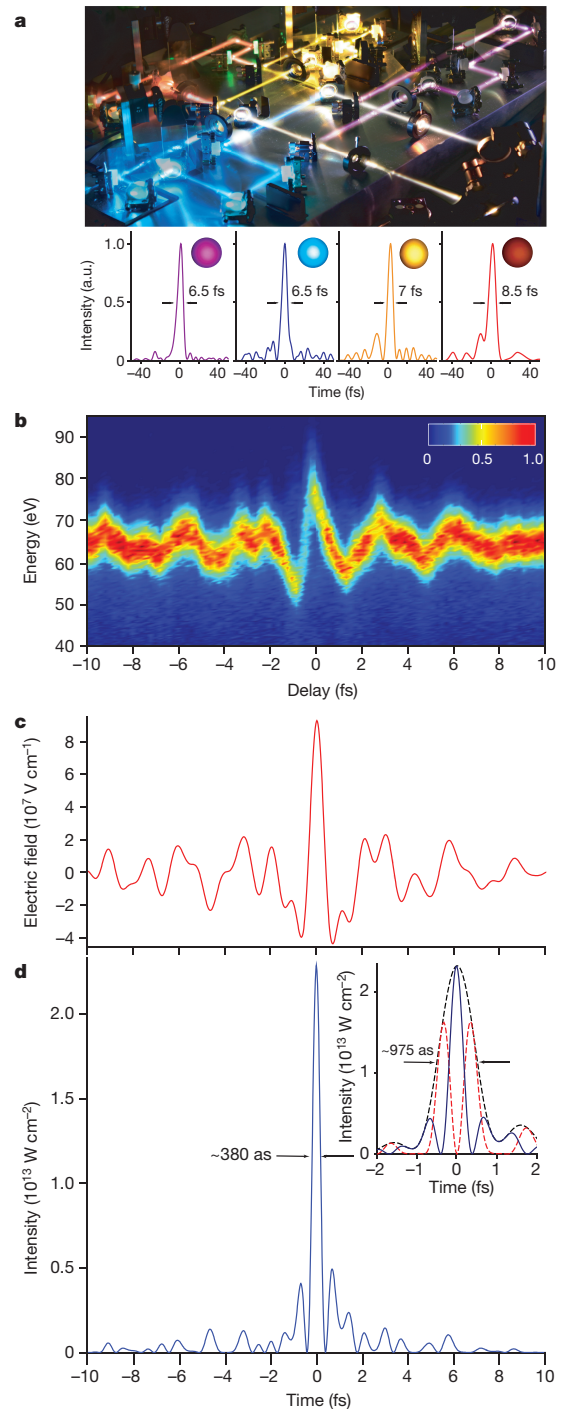


Figure 2 | Synthesis of an optical attosecond pulse. **a**, Photograph of an attosecond light-field synthesizer (top). The beams (artificially visualized) of ultra-wide-band pulses (about 1.1–4.6 eV) are divided by dichroic beam-splitters into four, almost equally wide, spectral bands. The pulses in each band are compressed so that they have durations of a few femtoseconds (the temporal intensity profiles are shown in the bottom panels), before they are spatiotemporally superimposed to yield a single beam/pulse at the exit of the apparatus. The insets in the bottom panels show representative beam profiles in the far field. **b**, Attosecond-streaking spectrogram of an optical attosecond pulse. The colour bar represents the yield of photoelectron counts in arbitrary units. **c, d**, Evaluated electric field (**c**) and instantaneous intensity profile (**d**; blue line) of the pulse. The intensity profile has a FWHM duration of approximately 380 as. The inset of **d** shows a close-up of this instantaneous intensity profile (blue line, $\phi_G \approx 0$) along with that of the same pulse, but with $\phi_G \approx \pi/2$ rad (dashed red line), and their common intensity envelope (dashed black line), which has a FWHM duration of approximately 975 as.

Phase-gating²¹ methods have successfully been used for tracing ionized-electron dynamics. To determine whether these methods can be extended to trace bound-electron dynamics with optical attosecond pulses, we simulate nonlinear dipole spectra as a function of the global phase ϕ_G of the optical attosecond pulse using the adiabatic model ($\rho_{\text{ad}}(\omega, \phi_G)$, Fig. 1b, right panel) and the TDSE model ($\rho_{\text{TDSE}}(\omega, \phi_G)$, Fig. 1c, right panel). The instantaneity of the nonlinear response underlying the adiabatic model (Fig. 1b, left panel) results in uniform spectral modulations of the emitted radiation with ϕ_G (Fig. 1b, right panel, shown for the range 5.7–8.2 eV to ease comparison with experiments). Indeed, the noticeable deviation between the instantaneous and TDSE time-domain nonlinear dipoles (Fig. 1d, e), and the dependence of this deviation on ϕ_G , give rise to easily discernible features in the corresponding spectrogram (Fig. 1c, left panel). These features are the manifestation of the delayed nonlinear response and include the non-synchronous amplitude modulation of the emitted frequencies with global phase (highlighted by the white dashed line) and the non-monotonic variation of the amplitude of the spectral emission along the energy axis.

We describe the nonlinear response of bound electrons in Kr with a simple heuristic model that expresses the nonlinear dipole $\rho(t, \phi_G)$ as a sum of instantaneous and delayed nonlinearities:

$$\rho(t, \phi_G) = aE^3(t, \phi_G) + bE^5(t, \phi_G) + cE^5(t - dt, \phi_G) \quad (1)$$

where a , b and c are coefficients, dt represents a delay and $E(t, \phi_G)$ is the electric field of the optical attosecond pulse for a global phase ϕ_G (see Methods). Provided $E(t, \phi_G)$ is known, equation (1) allows retrieval of the complete nonlinear dipole $\rho(t, \phi_G)$ from the numerical reconstruction of the corresponding ϕ_G spectrogram (Fig. 1c, right panel). This procedure underlines the suitability of the model for retrieving the nonlinear bound-electron response, and is instrumental for unveiling such dynamics from the experiments presented below.

To experimentally study the sub-femtosecond nonlinear response of bound electrons to light fields, we synthesized optical attosecond pulses. Two major advances of our synthesis method with respect to previously used methods^{22,23} have enabled the confinement and manipulation of optical pulses to <1 fs. First, the development of a second-generation light-field synthesizer (Fig. 2a), which extends optical synthesis to the deep ultraviolet range and manipulates pulses with spectra extending over more than two optical octaves over the visible and neighbouring ranges (about 1.1–4.6 eV), was crucial. Second, and equally important, was the realization of a broadband and virtually dispersion-free spectral equalization of the synthesized pulses, to give pulses with twice the initial bandwidth (see Methods section ‘Optical attosecond pulse synthesis’). These advances allow synthesis of optical attosecond pulses, which are highly energetic (about 50 μJ) and several

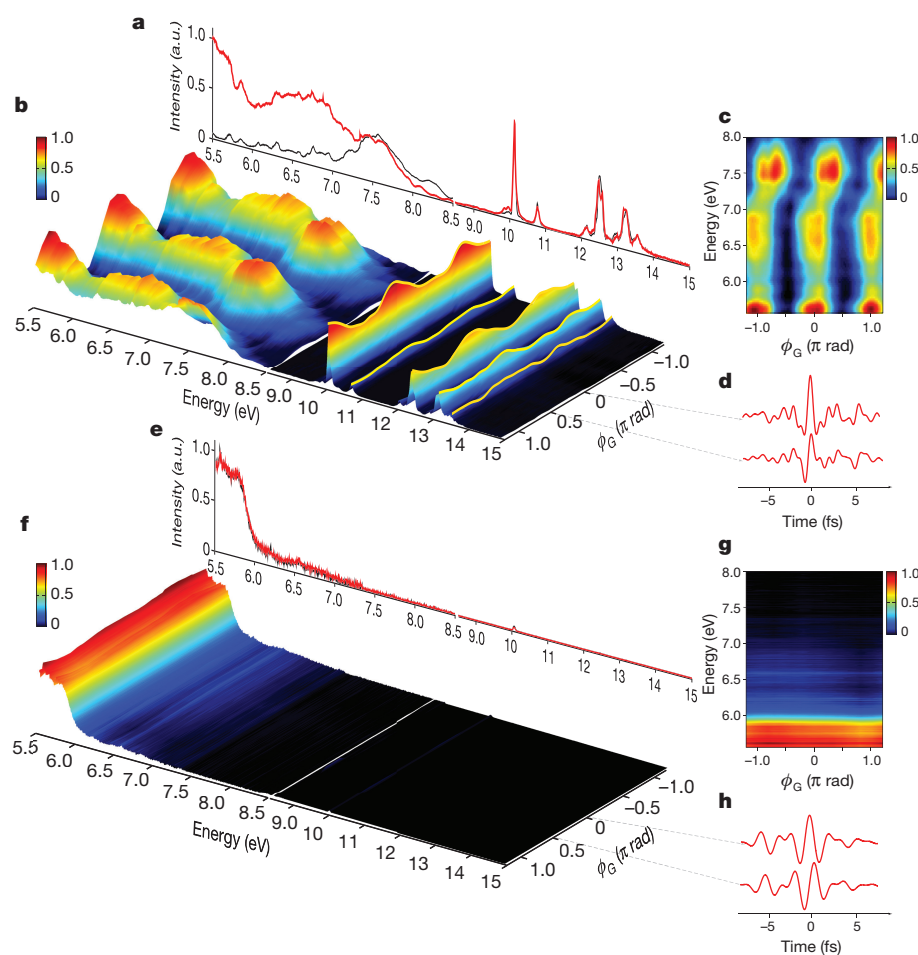


Figure 3 | Attosecond control of bound electrons in Kr. **a, e**, VUV spectra generated in neutral Kr atoms driven by an optical attosecond pulse (**a**) and a single-cycle pulse (**e**) of the same peak intensity (about $5 \times 10^{13} \text{ W cm}^{-2}$), at global phase settings of $\phi_G \approx 0$ (red line) and $\phi_G \approx \pi/2$ rad (black line). **b, f**, Spectrograms composed of 25 VUV spectra

(about 5.5–15 eV) recorded as a function of ϕ_G for an optical attosecond pulse (**b**) and a single-cycle pulse (**f**). **c, g**, Sections (about 5.5–8 eV) of the global-phase spectrograms in **b** and **f**, respectively. **d, h**, Representative driving waveforms at $\phi_G \approx 0$ (**d**) and $\phi_G \approx \pi/2$ rad (**h**). The colour scales in **b, c, f** and **g** indicate intensity (in arbitrary units).

orders of magnitude more intense (about 50 GW) than those obtainable with current extreme-ultraviolet (EUV) technology²⁴.

Figure 2b shows a representative streaking spectrogram of an optical attosecond pulse. The field waveform (Fig. 2c) retrieved from the data reveals a nearly isolated, half-cycle peak (centroid wavelength of approximately 530 nm), which has an intensity (Fig. 2d) approximately five times that of the adjacent peaks and carries more than about 50% of the energy of the waveform. The instantaneous intensity profile of the dominant half-cycle in Fig. 2d has a full-width at half-maximum (FWHM) duration of approximately 380 as, whereas an evaluation based on the conventional definition of the intensity envelope (Fig. 2d inset, dashed black line) yields a FWHM of approximately 975 as.

In our experiments (see Extended Data Fig. 1b), we probe the nonlinear polarization response of Kr atoms to optical attosecond pulses by recording the generated vacuum-ultraviolet (VUV) spectra. As shown in Fig. 3a, the spectra are quasi-continuous in the 5.5–10 eV range and exhibit discrete peaks coinciding with Kr excited-state energies in the 10–15 eV range. Variation of the global phase ϕ_G of the pulses yields a pronounced broadband modulation of the VUV emission (Fig. 3b), verifying our TDSE model predictions (Fig. 1c, right panel). In contrast, a pulse synthesized to consist of approximately a single optical cycle of commensurable intensity fails to generate broadband nonlinear excitation or its ϕ_G control (Fig. 3e–g). These results clearly demonstrate that in the absence of the extreme nonlinearities that arise under conditions of ionization, optical attosecond pulses are the key to manipulating bound electrons on a sub-femtosecond timescale.

The non-uniform modulation of the amplitude of the emitted dipole spectra (Fig. 3c) with ϕ_G and the uneven distribution of spectral amplitudes along the energy axis differ from the predictions of the adiabatic model for the same driving waveform (Fig. 1b, right panel), but resemble key features of the spectrograms constructed using TDSE simulations (Fig. 1c, right panel). These features offer experimental evidence of the non-instantaneous character of the response of the bound electrons of Kr in our experiments.

To apply the methodology presented above to retrieve the dynamics of the bound-electronic response, we supplemented our measurements with attosecond streaking of the driving field $E(\tau, \phi_G)$. By studying the dependence of the VUV emission as a function of the intensity of the optical driver, we verified that bound-electronic nonlinearities dominate the response (see Methods). Figure 4 shows the measured (left panels) and the corresponding reconstructed (right panels) spectrograms recorded at gradually increasing optical-field intensities: about $5 \times 10^{13} \text{ W cm}^{-2}$ (Fig. 4a); about $7 \times 10^{13} \text{ W cm}^{-2}$ (Fig. 4b); and about $9 \times 10^{13} \text{ W cm}^{-2}$ (Fig. 4c). The retrieved nonlinear dipoles (Fig. 4d) exhibit delays with respect to the instantaneous dipole (black line) and driving field $E(\tau, 0)$ (red dashed line) of $\tau \approx 45 \pm 4$ as (Fig. 4a), $\tau \approx 70 \pm 5$ as (Fig. 4b) and $\tau \approx 115 \pm 7$ as (Fig. 4c). The data in Fig. 4d verify the attosecond control of the bound-electronic response induced by the field, and emphasize the non-trivial character of the induced dynamics, which is manifested by a non-uniform delay (chirp). The latter is highlighted by the delay values for consecutive half-field-cycles shown in Fig. 4e. These findings, which are in excellent agreement with the predictions of the TDSE simulations performed for identical excitation fields, provide conclusive evidence for the feasibility of tracing and control of the nonlinear response of bound electrons on a sub-femtosecond timescale with high fidelity.

The findings of this study are compatible with an intuitive physical picture of the delayed nonlinear response, which we can now extend from the femtosecond molecular scale¹⁶ to attosecond electron dynamics. The optical-field-induced superposition of the ground state and excited states—which are typically more polarizable because the electron resides further from the atomic core—gives rise to an increase in the total nonlinear polarizability of the electron cloud during its interaction with the field. But this superposition requires a finite time to evolve, resulting in a delay in the nonlinear response of the system.

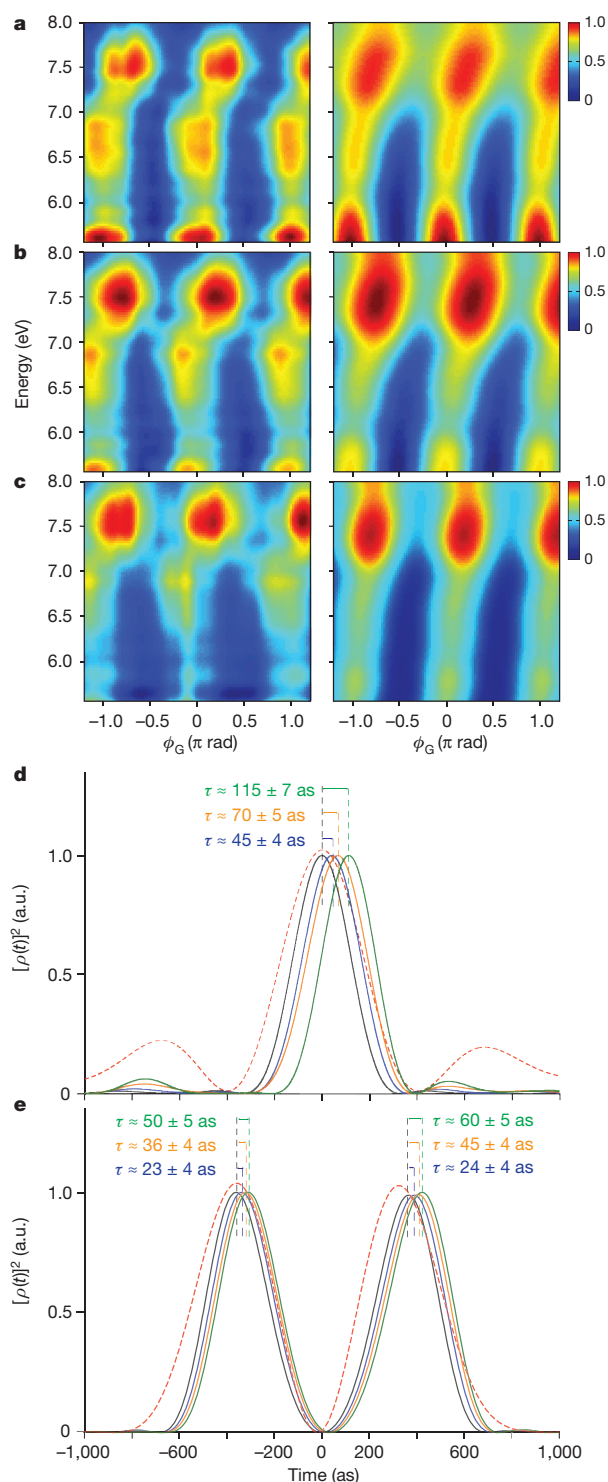


Figure 4 | Sub-femtosecond, delayed nonlinear response of bound electrons in Kr. a–c, Global-phase spectrograms of the optical attosecond pulse recorded at peak-intensity settings of about $5 \times 10^{13} \text{ W cm}^{-2}$ (a), $7 \times 10^{13} \text{ W cm}^{-2}$ (b) and $9 \times 10^{13} \text{ W cm}^{-2}$ (c) are shown in the left panels. Corresponding reconstructed spectrograms based on equation (1) are shown in the right panels. The colour bar represents spectral intensity in arbitrary units. d, e, Low-pass-filtered (0–8 eV) nonlinear dipoles obtained using the intensity settings in a–c (dark blue, orange, green lines, respectively) are shown along with the instantaneous response (black line) simulated for global-phase settings of the optical attosecond pulse of $\phi_G \approx 0$ (d) and $\phi_G \approx \pi/2$ rad (e). Standard errors of the mean for the delays (τ) indicated are evaluated from the reconstruction of three data sets recorded under identical experimental conditions. The dashed red lines are the normalized instantaneous intensities of the input electric fields.

Because both the amplitude of this superposition and the Stark shift²² of the induced electronic dipoles scale with field strength, the delay in the nonlinear response will also increase, in agreement with our theoretical and experimental studies.

It should be possible to extend the approach demonstrated here to the condensed phase. This will allow the electronic response in the bulk of complex systems subjected to strong fields to the probed^{14,25,26}, and will enable the possibility to trace electronic dephasing in such systems. By providing a probe, which is as short as the lifetime and dephasing times of core-hole electronic states in solids generated under attosecond X-ray excitation¹⁵, our tools could provide new ways to explore the nonlinear properties of X-ray excited solids. These novel spectroscopic capabilities may turn out to be instrumental—among others—to exploring the ultimate frontiers of electromagnetic signal processing in optical and X-ray regimes.

Online Content Methods, along with any additional Extended Data display items and Source Data, are available in the online version of the paper; references unique to these sections appear only in the online paper.

Received 10 June; accepted 3 December 2015.

1. Sheik-Bahae, M., Hutchings, D. C., Hagan, D. J. & Van Stryland, E. W. Dispersion of bound electron nonlinear refraction in solids. *IEEE J. Quantum Electron.* **27**, 1296–1309 (1991).
2. Boyd, R. W. *Nonlinear Optics* Ch. 1 (Academic Press, 1992).
3. Hentschel, M. *et al.* Attosecond metrology. *Nature* **414**, 509–513 (2001).
4. Niikura, H. *et al.* Sub-laser-cycle electron pulses for probing molecular dynamics. *Nature* **417**, 917–922 (2002).
5. Corkum, P. B. & Krausz, F. Attosecond science. *Nature Phys.* **3**, 381–387 (2007).
6. Schultze, M. *et al.* Delay in photoemission. *Science* **328**, 1658–1662 (2010).
7. Cavalieri, A. L. *et al.* Attosecond spectroscopy in condensed matter. *Nature* **449**, 1029–1032 (2007).
8. Goulielmakis, E. *et al.* Single-cycle nonlinear optics. *Science* **320**, 1614–1617 (2008).
9. Uiberacker, M. *et al.* Attosecond real-time observation of electron tunnelling in atoms. *Nature* **446**, 627–632 (2007).
10. Eckle, P. *et al.* Attosecond ionization and tunneling delay time measurements in helium. *Science* **322**, 1525–1529 (2008).
11. Shafir, D. *et al.* Resolving the time when an electron exits a tunnelling barrier. *Nature* **485**, 343–346 (2012).
12. Ivanov, M. & Smirnova, O. Opportunities for sub-laser-cycle spectroscopy in condensed phase. *Chem. Phys.* **414**, 3–9 (2013).
13. Krüger, M., Schenk, M. & Hommelhoff, P. Attosecond control of electrons emitted from a nanoscale metal tip. *Nature* **475**, 78–81 (2011).
14. Schiffrin, A. *et al.* Optical-field-induced current in dielectrics. *Nature* **493**, 70–74 (2013).
15. Schultze, M. *et al.* Controlling dielectrics with the electric field of light. *Nature* **493**, 75–78 (2013).
16. Weiner, A. M. *Ultrafast Optics* Ch. 6 (John Wiley & Sons, 2009).
17. Zewail, A. H. Femtochemistry: atomic-scale dynamics of the chemical bond. *J. Phys. Chem. A* **104**, 5660–5694 (2000).
18. Goulielmakis, E. *et al.* Real-time observation of valence electron motion. *Nature* **466**, 739–743 (2010).
19. Smirnova, O. *et al.* High harmonic interferometry of multi-electron dynamics in molecules. *Nature* **460**, 972–977 (2009).
20. Zewail, A. H. *Femtochemistry: Ultrafast Dynamics of the Chemical Bond* Vol. 1 (World Scientific, 1994).
21. Dudovich, N. *et al.* Measuring and controlling the birth of attosecond XUV pulses. *Nature Phys.* **2**, 781–786 (2006).
22. Wirth, A. *et al.* Synthesized light transients. *Science* **334**, 195–200 (2011).
23. Hassan, M. Th. *et al.* Invited Article: attosecond photonics: synthesis and control of light transients. *Rev. Sci. Instrum.* **83**, 111301 (2012).
24. Sansone, G., Poletto, L. & Nisoli, M. High-energy attosecond light sources. *Nature Photon.* **5**, 655–663 (2011).
25. Vampa, G. *et al.* Linking high harmonics from gases and solids. *Nature* **522**, 462–464 (2015).
26. Hohenleutner, M. *et al.* Real-time observation of interfering crystal electrons in high-harmonic generation. *Nature* **523**, 572–575 (2015).

Acknowledgements This work was supported by European Research Council grant (Attoelectronics-258501), the Deutsche Forschungsgemeinschaft Cluster of Excellence: Munich Centre for Advanced Photonics (<http://www.munich-photonics.de>), the Max Planck Society and the European Research Training Networks ATTOFEL and MEDEA, the Russian Foundation for Basic Research (projects numbers 13-02-01465, 13-02-92115 and 13-04-40335) and the Welch Foundation (grant number A-1801).

Author Contributions M.Th.H., T.T.L., A.M. and M.G. conducted the experiments; O.R. and V.P. developed the dispersive optics for the experiments; E.G. planned the experiments and supervised the project; M.Th.H., T.T.L., P.Z., A.M. and N.K. conducted the simulations; and M.Th.H., T.T.L., A.M., A.M.Z., F.K. and E.G. interpreted the data and contributed to the preparation of the manuscript.

Author Information Reprints and permissions information is available at www.nature.com/reprints. The authors declare no competing financial interests. Readers are welcome to comment on the online version of the paper. Correspondence and requests for materials should be addressed to E.G. (elgo@mpq.mpg.de).

METHODS

Optical attosecond pulse synthesis. Light waveforms whose spectra extend over more than two optical octaves in the visible and adjacent spectral range (about 1.1–4.6 eV) (Extended Data Fig. 1a) are generated by the nonlinear broadening of laser pulses (approximately 22 fs, 1 mJ, 790 nm) through a hollow-core fibre (HCF) filled with Ne gas (about 2.3 bar). The energy of the generated supercontinuum at the exit of the HCF is about 550 μ J. The spectra of these pulses are divided by dichroic beam-splitters into four almost equally wide spectral bands centred in the near infrared (NIR; about 1.1–1.75 eV), visible (vis; about 1.75–2.5 eV), visible-ultraviolet (vis-UV; about 2.5–3.5 eV) and deep ultraviolet (DUV; about 3.5–4.6 eV). The pulses in these bands are individually compressed by dispersive mirrors to durations of a few femtoseconds before they are spatially and temporally superimposed to yield a single beam/pulse at the exit of the apparatus. The pulses are temporally characterized by a transient-grating frequency-resolved optical gating (TG-FROG) apparatus. The durations T of the pulses in different channels of the synthesizer were measured to be $T_{\text{NIR}} \approx 8.5$ fs, $T_{\text{vis}} \approx 7$ fs, $T_{\text{vis-UV}} \approx 6.5$ fs and $T_{\text{DUV}} \approx 6.5$ fs (see inset to Fig. 2a). The synthesizer apparatus transmits about 82% of the energy of the incoming supercontinuum. As a result, the pulse energy at the exit of the apparatus is about 320 μ J, and is distributed among the four channels as $\text{Ch}_{\text{NIR}} \approx 255$ μ J, $\text{Ch}_{\text{vis}} \approx 45$ μ J, $\text{Ch}_{\text{vis-UV}} \approx 15$ μ J and $\text{Ch}_{\text{DUV}} \approx 4$ μ J, where Ch_i denotes the energy of channel i .

For the synthesis of optical attosecond pulses, both precise control of the relative delay between the constituent pulses in the synthesizer as well as an intensity control over the spectral channels is required. To this end, we followed a new approach, which effectively enables the passive spectral intensity control and facilitates the attosecond streaking characterization of the generated optical waveforms in the same set-up. The EUV attosecond probe is generated first (Extended Data Fig. 1b) by focusing the light transients from the synthesizer into a quasi-static Ne gas cell. The EUV radiation, which emerges collinearly to the driver waveform, is transmitted through a thin, round Zr foil, while the optical pulse, which is transmitted around the geometrical margins of this foil, forms an annular beam. A double-mirror module consisting of a concave, multilayer, coated inner mirror and a metal–dielectric–metal (MDM)-coated concave annular sector (outer mirror) (Extended Data Fig. 2) of the same focal length ($f = 12.5$ cm), focuses the light transients and the EUV attosecond probe into a second Ne gas nozzle placed near the entrance of a time-of-flight (TOF) spectrometer (Extended Data Fig. 1b). One of the essential characteristics of the MDM is that the imposed spectral control results in negligible phase distortions over the whole spectral range of the supercontinuum pulse. This was experimentally verified by FROG measurements of the pulses in the constituent channels upon reflection off the MDM unit. At the same time, because the EUV probe is generated before the spectral intensity control of the optical transient, it overcomes a fundamental limitation of a half-cycle field: the efficient generation of intense EUV-probe pulses. This is because a half-cycle field does not involve at least two intense field crests, which are required for ionization and subsequent acceleration of electrons²⁷ leading to high harmonic generation.

Single-cycle optical pulses are generated by physically suppressing a part (>3 eV) of the high-frequency spectrum of the optical attosecond pulse.

Generation of VUV spectra. We focus optical attosecond pulses into a quasi-static cell, which replaces the Ne gas jet used for performing attosecond-streaking characterization of their fields, filled with Kr atoms at a moderate pressure (about 80 mbar) (Extended Data Fig. 1b). We probe the nonlinear polarization of the system by recording VUV spectra that emerge collinearly with the driving optical field using a spectrometer placed downstream from the cell. The spectra are sampled at energies higher than about 5 eV, that is, beyond the constituent spectrum of the optical attosecond pulses, and extend no higher than the ionization threshold of neutral Kr ($I_p \approx 14$ eV).

Ultimate limit of carrier-envelope phase decomposition. The concept of the carrier-envelope phase ϕ_{CE} (CEP) is most readily understood in the time domain²⁸. The carrier-envelope phase is the interval Δt_{peak} between the maximum of the envelope and the maximum of the instantaneous field, translated in phase at the centroid frequency ω_L of the spectrum: $\phi_{\text{CE}} = \omega_L \times \Delta t_{\text{peak}}$. Any electric field can be decomposed, according to Hilbert's transform as

$$E(t) = A(t) \cos(\omega_L t + \phi_G)$$

in which $A(t)$ is the envelope (the modulus of the analytical field) and ϕ_G is the global (or absolute) phase.

The maximum of the field is determined by solving

$$\dot{E}(t) = 0 \Leftrightarrow \frac{\dot{A}(t)}{\omega_L A(t)} = \tan(\omega_L t + \phi_G) \quad (2)$$

On the basis of this equation and the estimation $\frac{\dot{A}(t)}{\omega_L A(t)} \approx \frac{\Delta\omega}{\omega_L}$, we distinguish two different regimes:

(1) For pulses with durations longer than one cycle, $\Delta\omega / \omega_L = 1$ and the solution of equation (2) yields $\phi_G = \omega_L \times \Delta t_{\text{peak}} = \phi_{\text{CE}}$, which confirms the equivalence between the global (ϕ_G) and carrier-envelope (ϕ_{CE}) phases.

(2) For sub-cycle pulses, $\Delta\omega / \omega_L > 1$ and so the solution of equation (2) is not trivial because, in a fraction of a cycle, the envelope varies substantially. Consequently, $\omega_L \times \Delta t_{\text{peak}} < \phi_G$ and the global and carrier-envelope phases are no longer equivalent.

Extended Data Fig. 3a presents the case of a half-cycle pulse—an optical attosecond pulse. The sinusoidal waveform (red) reaches its maximum at 0.2 periods instead of 0.25, which is expected for a wave with a phase of $\pi/2$ rad. Extended Data Fig. 3b shows the CEP determined using the method of the field maximum depending on the pulse duration, for three settings of the global phase. This comparison reveals a considerable difference between ϕ_{CE} and ϕ_G in the short pulse regime. In view of the above justification, it is clear that the CEP is an accurate description of the global phase only for pulses longer than one cycle.

Time-dependent Schrödinger equation and adiabatic models. To theoretically study the nonlinear dipole dynamics in Kr atoms exposed to intense optical attosecond pulses, we used two models. In the first, we solve the three-dimensional time-dependent Schrödinger equation (TDSE) within the single-active-electron approximation. To this end, we used a central potential for Kr, which was calculated using optimized effective-potential methods²⁹. In the second, and in order to describe instantaneous response, we assumed an adiabatic model based on a two-level system^{12,30}, in which the dipole moment, in the quasi-static approximation, can be expressed as:

$$\rho(t) = \frac{2d^2 E(t)}{\sqrt{4d^2 [E(t)]^2 + \omega_0^2}}$$

where d is chosen to match the nonlinear polarizability of Kr (refs 31, 32), ω_0 is the excitation energy $\hbar\omega_0 \approx 10$ eV and $E(t)$ denotes the electric field of the optical attosecond pulse. To access the nonlinear component of the induced electronic dipole moment at a given intensity of the driving field in both models, we perform a second calculation at a much lower (about six orders of magnitude) intensity. As a next step, we subtract the virtually linear dipole calculated at the lower intensity from the original one, after multiplying it by the corresponding ratio between the two intensities. The calculated global-phase spectrograms (spectral emission as a function of the global phase) using the adiabatic and TDSE models are shown in Extended Data Fig. 4a, b. In accordance with the discussion in the main text, the adiabatic model (Extended Data Fig. 4a) predicts uniform modulations of the spectral amplitude of the emitted spectral components as a function of the global phase ϕ_G . In contrast, the spectrogram calculated using the TDSE model embodies the signatures of the delayed electronic response (Extended Data Fig. 4b) in the form of asynchronous amplitude modulations between different frequencies/energies of the emitted dipole. These features are present in the entire emitted spectrum, not only close to the resonant area (10–14 eV). We show that these effects can be used to extract the dynamics of the nonlinear response by reconstructing the global-phase (ϕ_G) spectrograms recorded in our experiments.

Extended Data Fig. 4c shows a global-phase spectrogram simulated for a single-cycle pulse using the TDSE Kr model. In this regime of single-cycle pulses, the global-phase spectrogram does not show discernible variation over ϕ_G , which is experimentally verified (see Fig. 3e–g).

Ionization-free strong field polarization of bound electrons. An essential innovation introduced by using optical attosecond pulses is their unique capability to drive nonlinear dynamics in quantum systems without inducing a substantial degree of ionization or excitation, that is, without greatly altering the original system. In experiments where the polarization of the system is to be probed, both excessive ionization and excitations markedly modify the system, resulting in a considerable degree of ‘contamination’ in the emitted signal from the new atomic entities; such contamination is challenging to resolve both experimentally and theoretically.

This capability is unique to isolated sub-cycle pulse structures and is not observed for trains of sub-cycle field modulation³³ because the nanosecond-long exposure of atoms to such fields yields a substantial degree of ionization, which is actually the means to trace the waveform in these experiments³⁴. The ionization and excitation probability of Kr atoms calculated by the solution of the TDSE and the waveform used in our experiments for a range of intensities (summarized in Extended Data Table 1) verify this conjecture. Experimentally, we also verified this fact by using the previously established and highly sensitive technique of attosecond transient absorption spectroscopy¹⁸.

The interaction of optical attosecond pulses with matter, even at excessive intensities such as those used in our experiments and simulations, can be mostly considered as a scattering process. The system and the pulse virtually do not exchange energy; rather, the pulse probes the system via nonlinear scattering and the emission of coherent radiation.

Nonlinearities in the interaction of Kr with intense optical attosecond pulses. Identifying the dominant nonlinearities in the interaction between the optical attosecond pulses and the Kr atoms, and understanding the dependence of these nonlinearities on the variation of the global phase (ϕ_G) of the optical attosecond pulse—the key control point of the interaction in experiments with such waveforms—is essential for the development of intuitive models that can describe the nonlinear dynamics. As we show below, it allows the development of a robust methodology that permits the reconstruction of the dynamics of the response from global-phase spectrograms.

To this end, we theoretically (using TDSE simulations in Kr) studied the intensity dependence of the yield of the spectral emission (averaged over the range 0–8 eV) under optical attosecond pulses for the range of intensity settings used in our experiments. The corresponding nonlinearities can be evaluated from the slope of the linear fit of the data in the log–log diagram of Extended Data Fig. 5. A linear fitting over the entire range of intensities studied (2×10^{13} – 10×10^{13} W cm⁻²) reveals a slope of about 4, and suggests the dominance and coexistence of the two most essential nonlinearities in centrosymmetric systems: the third- (E^3) and the fifth- (E^5) order nonlinearities—broadly known as bound-electronic nonlinearities.

Simple model of the field-driven bound-electron nonlinear response of Kr. The study presented in the previous paragraph highlights the dominance of bound-electron nonlinearities in the response and the low or negligible sensitivity of the nonlinearity to the global phase of our pulses.

To account for the non-instantaneous response revealed in our TDSE simulations, and inspired by previous approaches in ultrafast spectroscopy³⁵, in which the nonlinear response is decomposed into instantaneous and delayed components, we describe the nonlinear dipole moment as a sum over instantaneous third- and fifth-order nonlinearities, as well as the fifth-order delayed nonlinearity according to equation (1):

$$\rho(t, \phi_G) = aE^3(t, \phi_G) + bE^5(t, \phi_G) + cE^5(t - dt, \phi_G)$$

Here, a , b and c are coefficients, dt represents a delay of the fifth-order response and $E(t, \phi_G)$ is the electric field of the optical attosecond pulse for a global phase ϕ_G .

One would generally expect delayed terms to be considered for all nonlinearities involved (including the third-order); the energy diagram of Extended Data Fig. 6 offers an intuitive explanation of our choice to limit the delayed terms to only fifth-order nonlinearities. Indeed, delayed response in the range 0–9 eV will primarily involve virtual transitions, which can coherently couple at least two electronic states of the system (ground and excited states or combinations of excited states). The diagram demonstrates this assuming virtual transition compatible with the energy spectrum of our optical attosecond pulse (1.1–4.6 eV). Such transitions can only occur within the fifth-order response (higher-order Kerr effects). The diagram also highlights—through the multiphoton picture—that at this extreme limit of pulse duration and corresponding bandwidth, non-resonant and resonant response are virtually inseparable. As a result, the coherent dynamics induced between two or more states of the system will be manifested at each nonlinearly emitted spectral component in the process.

Extended Data Fig. 7a–c shows representative, synthetic, global-phase spectrograms for three values of the parameter dt ($dt=0$ (instantaneous response), $dt=20$ as and $dt=30$ as), generated by equation (1) in the spectral range of our experiments (see Fig. 4). The synthetic spectrograms highlight the capability of the model to capture key features of the experimental spectrograms (for example, Figs 1 or 4), such as the profoundly asynchronous modulation of the emission in the range 7–8 eV and the weakening of the amplitude in the range 6–6.5 eV—both are the result of dynamic nonlinear interference between delayed and instantaneous terms in equation (1).

To further verify the validity of our model, we used the TDSE simulations in Kr as a basis to explore how a dipole described by the above equations could represent the (below resonances) nonlinear response of the system.

Extended Data Fig. 7d shows the TDSE simulated dipoles (black line) and their fitting with equation (1). We investigated both the capability of the model to fit only a fraction (spectrally filtered from 5.5–8 eV; Extended Data Fig. 7d) of

the dipole as well the entire dipole (0–8 eV) below resonances (Extended Data Fig. 7e). A single set of the parameters a , b , c and dt in equation (1), and a given peak intensity of the pulse, can precisely reproduce the nonlinear dipole (black lines) for all settings of the global phase. Representative examples for two (extreme) settings of the global phase $\phi_G \approx 0$ (left panels of Extended Data Fig. 7d and e) and $\phi_G \approx \pi/2$ rad (right panels of Extended Data Fig. 7d and e) are shown. Furthermore, the parameters a , b , c and dt extracted from fitting part of the nonlinear spectrum (5.5–8 eV) (Extended Data Fig. 7d) are identical to those required to fit the entire range (0–8 eV) (Extended Data Fig. 7e). As a conclusion, even a limited fraction of the nonlinear spectrum contains information about the interfering terms in equation (1). The model works well for a wide range of peak intensities (not shown); therefore, we conclude that it is adequate for reconstructing the response.

Nonlinear dipole reconstructions. The most critical test of the capability of our model to reconstruct experimental data and to trace the time-domain nonlinear dipole dynamics, is to perform a numerical experiment. To do so, we create a theoretical spectrogram using the TDSE model (where the nonlinear dipole is known *a priori*) and attempt to reconstruct this nonlinear dipole using (i) equation (1), (ii) the spectrogram constructed by the TDSE simulation, and (iii) the *a priori* measured driver field waveform.

For both experimental and synthetic data, we used a quickly converging nonlinear algorithm to perform the reconstructions. It is based on a commercial, highly optimized numerical routine that uses the ‘trust-region’ method³⁶, which is usually used for constrained problems. The root-mean-square deviation (r.m.s.d.) was determined, and defined as the main parameter to optimize our reconstruction via its minimization. The r.m.s.d. is calculated as:

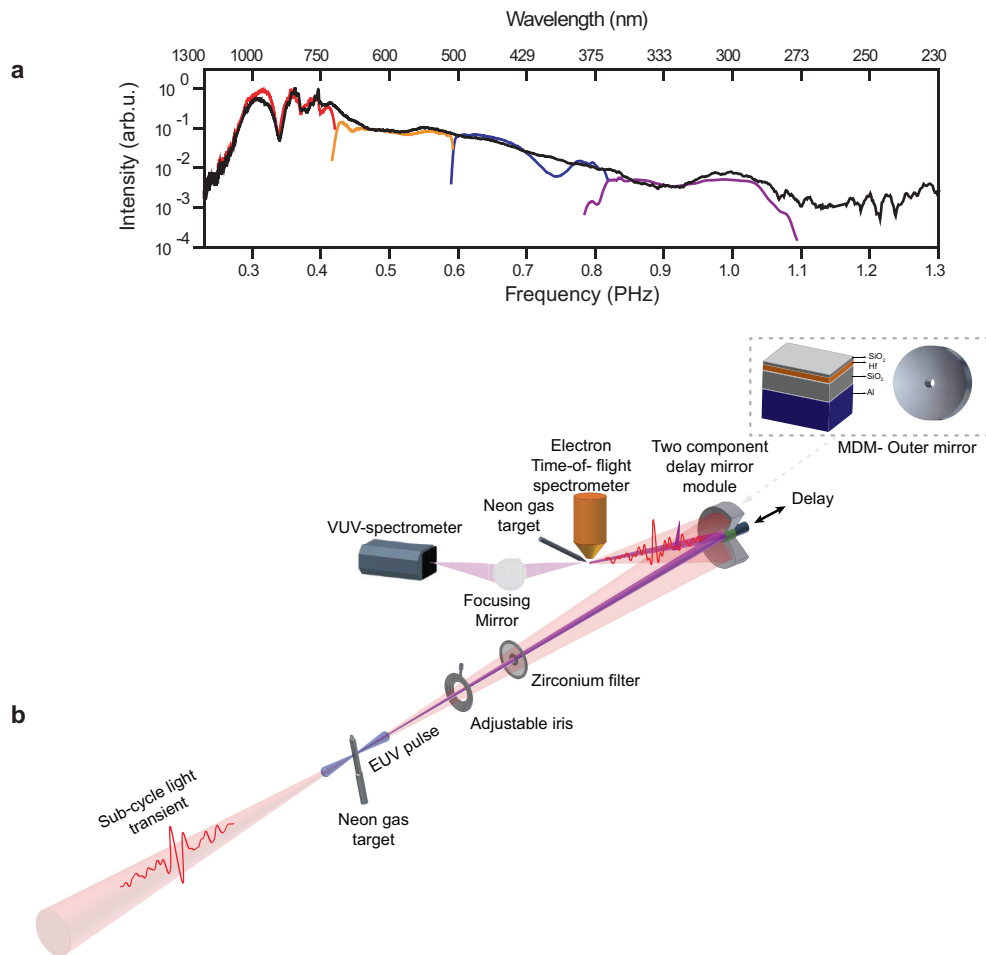
$$\text{r.m.s.d.} = \sqrt{\frac{\sum_{i=1}^{n_{\phi_G}} \int_{\omega_1}^{\omega_2} (\hat{X}_i - X_i)^2 d\omega}{n_{\phi_G} \times n_{\omega}}}$$

Where \hat{X} and X are the computed and original (measured) spectra, respectively, at certain global-phase settings, $\omega_1 = 5.5$ eV, $\omega_2 = 8$ eV, n_{ϕ_G} is the number of global-phase settings of the measured VUV spectrogram, and n_{ω} is the number of frequencies involved (from ω_1 to ω_2).

The results of this study are summarized in (Extended Data Fig. 8a, b), in which the original and the reconstructed spectrograms are shown. The reconstruction parameters in equation (1) are $a = 0.180$, $b = 0.096$, $c = -0.177$ and $dt = 67$ as. Extended Data Figure 8c, d compares the reconstructed (red line) and the *a priori* known nonlinear dipole (black line) for two different settings of the global phase. Blue lines show the instantaneous response for the same waveforms for comparison.

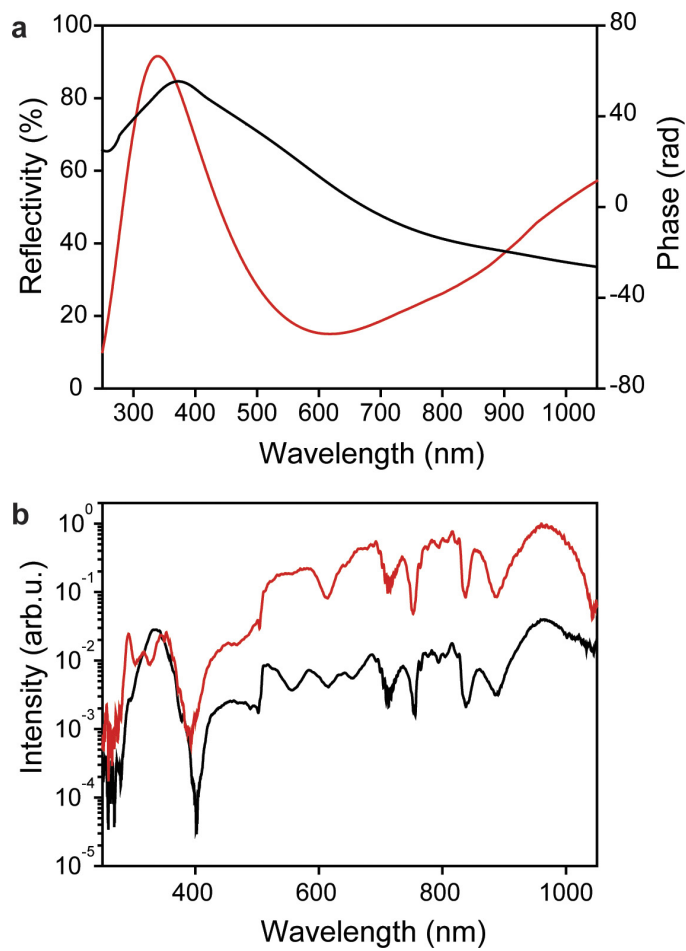
Intensity dependent nonlinear delay. We study the delayed nonlinear bound-electronic response over a wide range of intensities ($(2-8) \times 10^{13}$ W cm⁻²). The evaluated delays between the instantaneous and the TDSE-simulated dipoles as function of the driver field intensity are shown in Extended Data Fig. 9a; the delays between the instantaneous dipoles and those reconstructed from our measured spectrograms (see Fig. 4) are shown in Extended Data Fig. 9b.

- Corkum, P. B. Plasma perspective on strong field multiphoton ionization. *Phys. Rev. Lett.* **71**, 1994–1997 (1993).
- Krausz, F. & Ivanov, M. Attosecond physics. *Rev. Mod. Phys.* **81**, 163–234 (2009).
- Muller, H. G. An efficient propagation scheme for the time-dependent Schrödinger equation in the velocity gauge. *Laser Phys.* **9**, 138–148 (1999).
- Gauthey, F. I., Garraway, B. M. & Knight, P. L. High harmonic generation and periodic level crossings. *Phys. Rev. A* **56**, 3093–3096 (1997).
- Lundeen, T., Hou, S. Y. & Nibler, J. W. Nonresonant third order susceptibilities for various gases. *J. Chem. Phys.* **79**, 6301–6305 (1983).
- Shelton, D. P. Nonlinear-optical susceptibilities of gases measured at 1064 and 1319 nm. *Phys. Rev. A* **42**, 2578–2592 (1990).
- Harris, S. E. & Sokolov, A. V. Subfemtosecond pulse generation by molecular modulation. *Phys. Rev. Lett.* **81**, 2894–2897 (1998).
- Baker, S., Walmsley, I. A., Tisch, J. W. G. & Marangos, J. P. Femtosecond to attosecond light pulses from a molecular modulator. *Nature Photon.* **5**, 664–671 (2011).
- Blow, K. J. & Wood, D. Theoretical description of transient stimulated Raman scattering in optical fibers. *IEEE J. Quantum Electron.* **25**, 2665–2673 (1989).
- Coleman, T. F. & Li, Y. Y. An interior trust region approach for nonlinear minimization subject to bounds. *SIAM J. Optim.* **6**, 418–445 (1996).

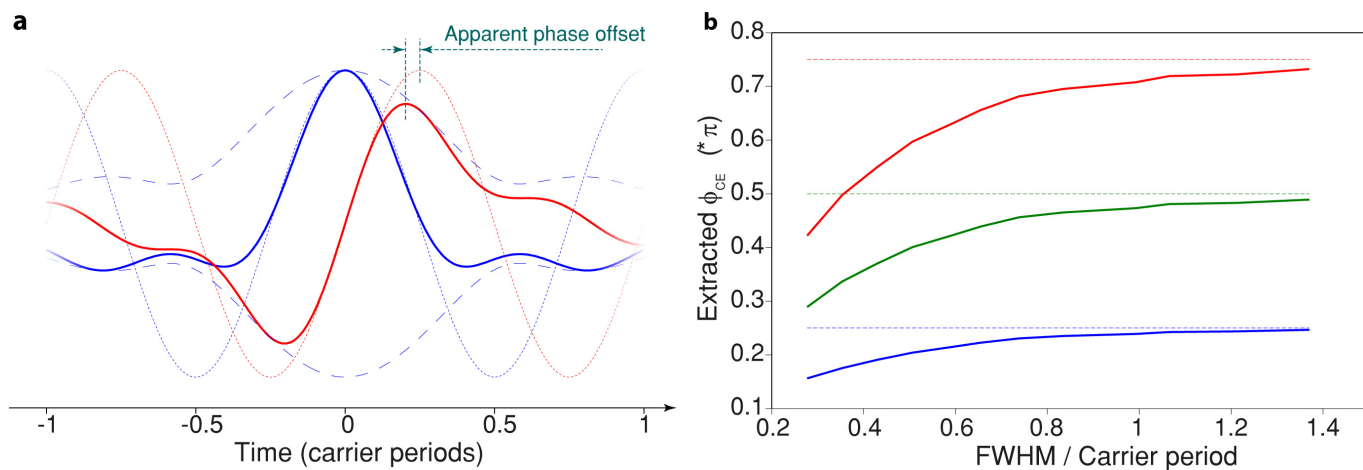


Extended Data Figure 1 | Supercontinuum spectra and experimental set-up. **a**, The supercontinuum spectra spans more than two octaves (1.1–4.6 eV), and is shown by the black line; the spectra of the individual

channels Ch_{NIR} , Ch_{vis} , Ch_{vis-UV} and Ch_{DUV} are shown by the red, orange, blue and violet lines, respectively. **b**, Schematic illustration of the experiment set-up.

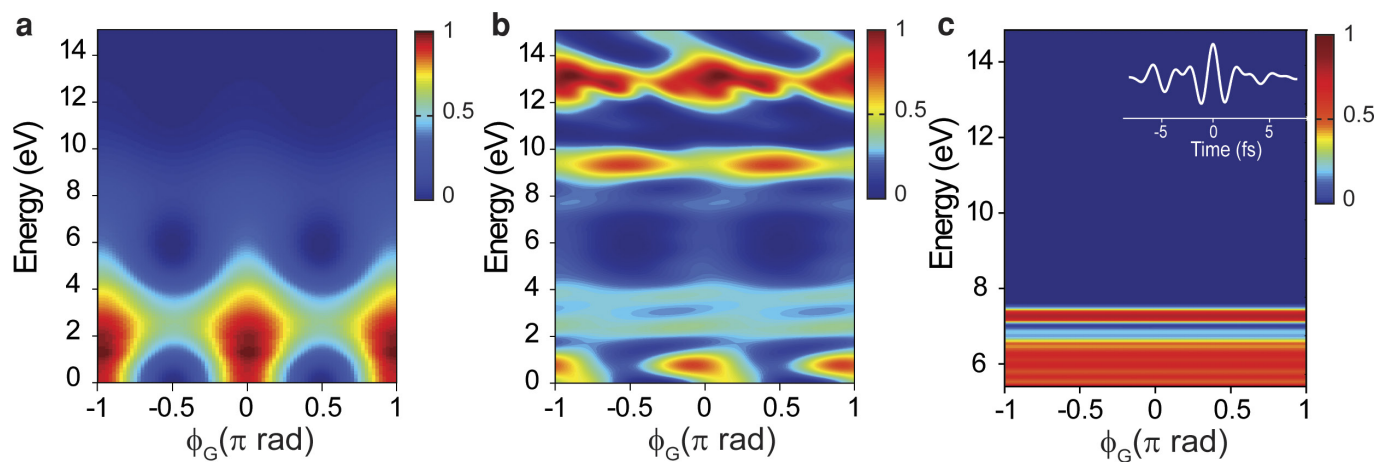


Extended Data Figure 2 | Spectral equalization by a metal-dielectric-metal (MDM) coating. **a**, The designed reflectivity (red line) and spectral phase (black) of the MDM coating applied on the outer mirror of the double mirror module shown in Extended Data Fig. 1. **b**, Multi-octave spectrum at the exit of the synthesizer (red line) and upon reflection off the MDM mirror (black line).



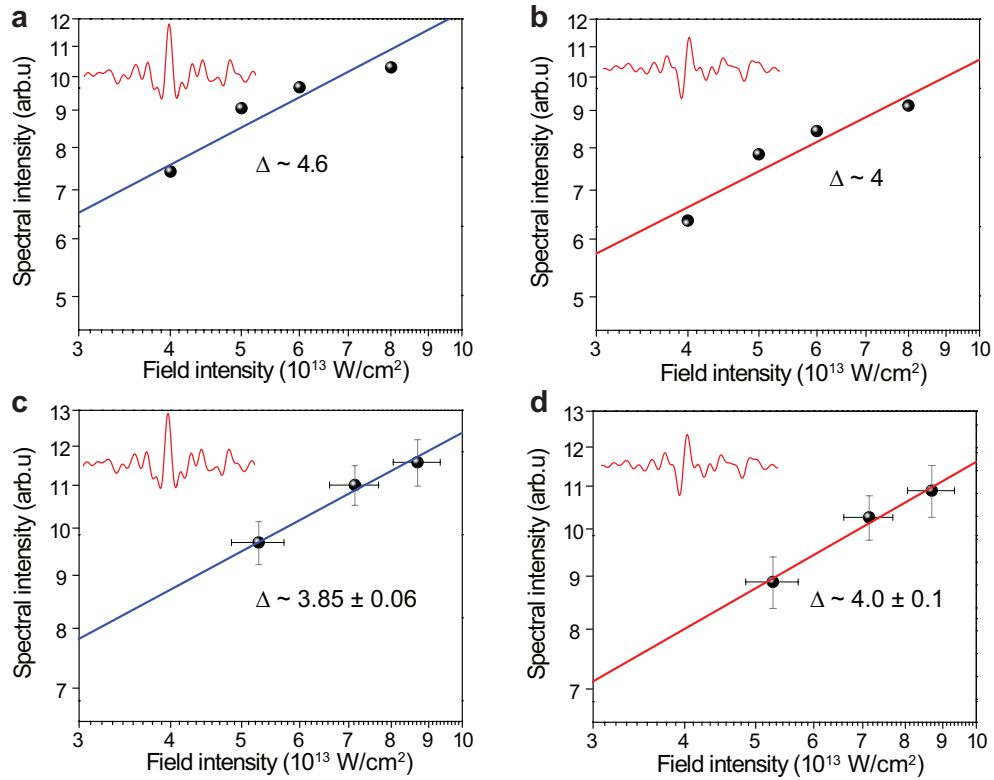
Extended Data Figure 3 | Global phase and CEP difference in a sub-cycle regime. a, Half-cycle, cosine-like (blue line) and sine-like (red line) waveforms, compared with the carrier wave (dotted blue and red lines) and envelope (dashed blue lines). **b,** Limits of CEP decomposition in the time

domain. Retrieved CEP (solid lines) versus global-phase offset (dashed lines) as a function of the ratio between the FWHM of the intensity envelope and the period of the carrier wave for $\phi_G = \pi/4$ rad (blue line), $\phi_G = \pi/2$ rad (green line) and $\phi_G = 3\pi/4$ rad (red).



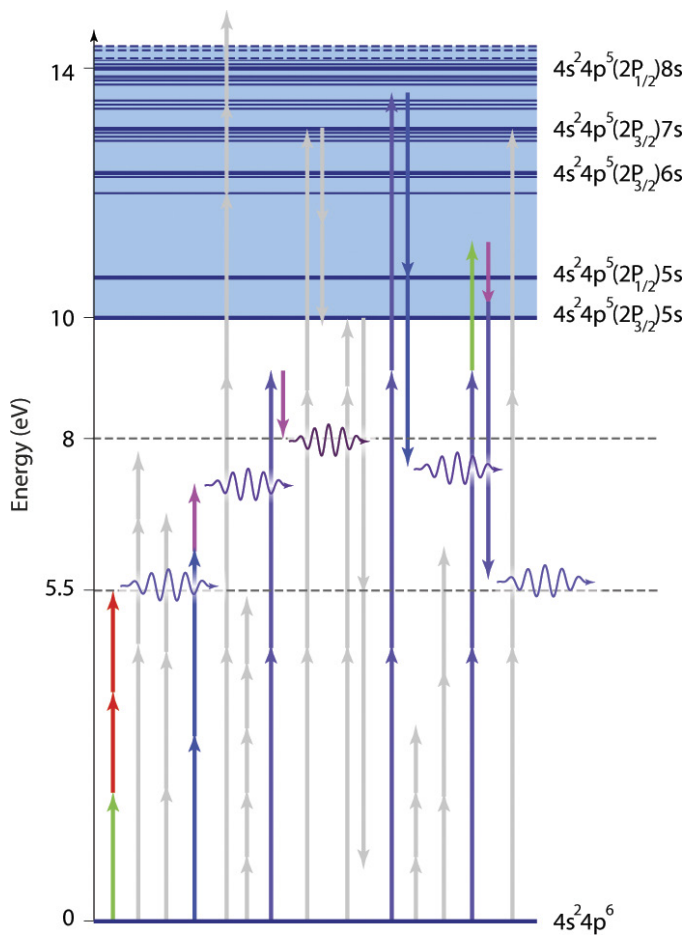
Extended Data Figure 4 | Simulated global-phase spectrograms.
a, b, Calculated global-phase (ϕ_G) spectrograms using the adiabatic model (**a**) and the TDSE model (**b**) for experimentally sampled waveforms (optical attosecond pulse) and an intensity of about $4 \times 10^{13} \text{ W cm}^{-2}$.

c, Simulated global-phase spectrograms for a sub-cycle pulse (about 2 fs; shown in inset). The polarization response is insensitive to global-phase variation of the waveform; see also experiments in Fig. 3. The colour scale represents the spectral intensity in arbitrary units.

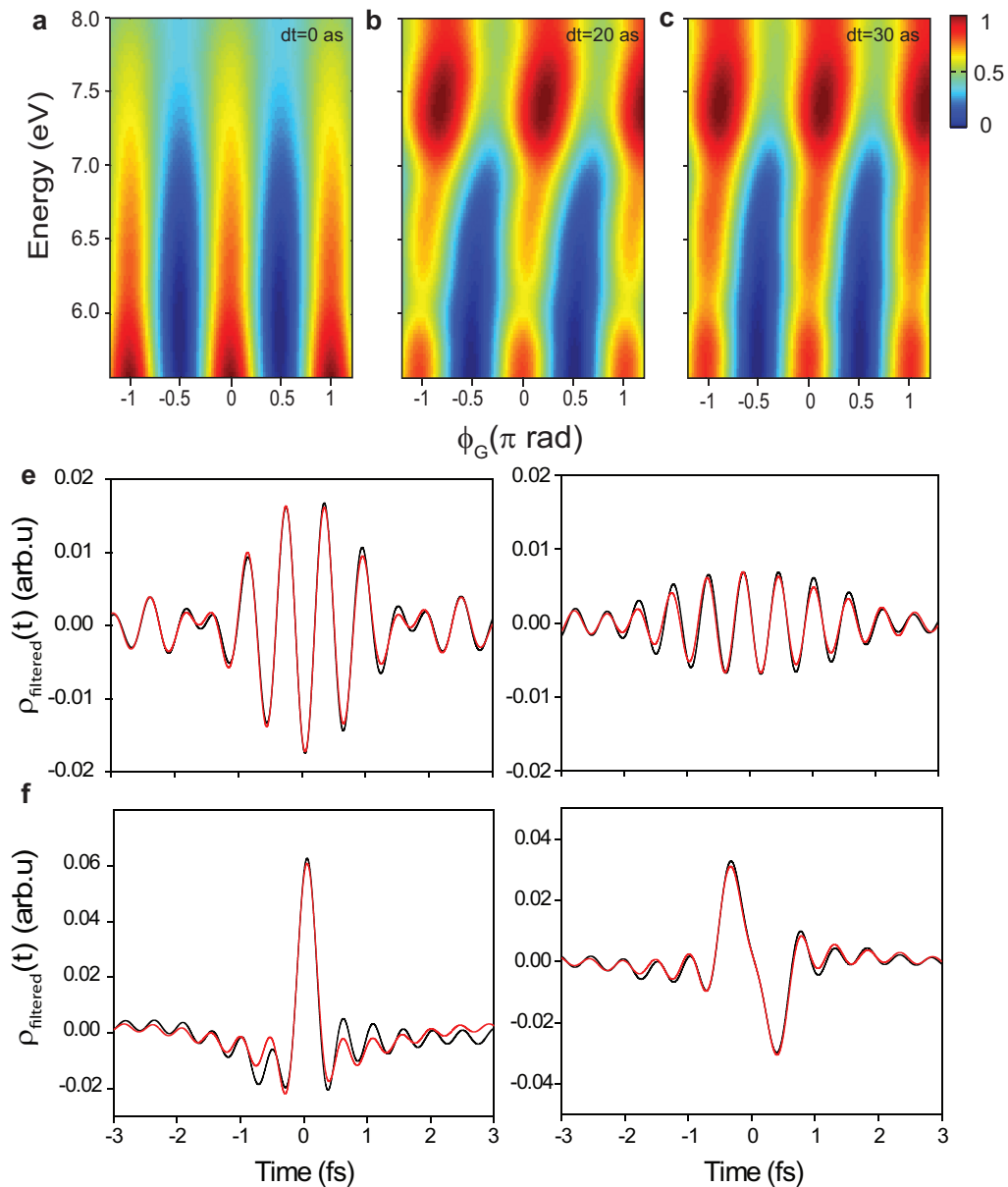


Extended Data Figure 5 | Nonlinearity study of the interaction of an optical attosecond pulse with a Kr atom. a–d, Data points show the spectrally integrated yield of the nonlinear polarization (0–8 eV) as a function of the intensity of the optical attosecond pulse for two global phases ϕ_G of the driving waveform, $\phi_G \approx 0$ (**a, c**) and $\phi_G \approx \pi/2$ rad (**b, d**),

evaluated from TDSE simulations (**a, b**) and our experiments in Fig. 4 (**c, d**). The error bars represent the standard error of the mean of the input field intensity and the calculated integrated spectral yield of the nonlinear polarization. Δ is the slope of the linear fitting of the log–log plots; the errors shown indicate the standard error of mean, with $n = 3$. Insets show

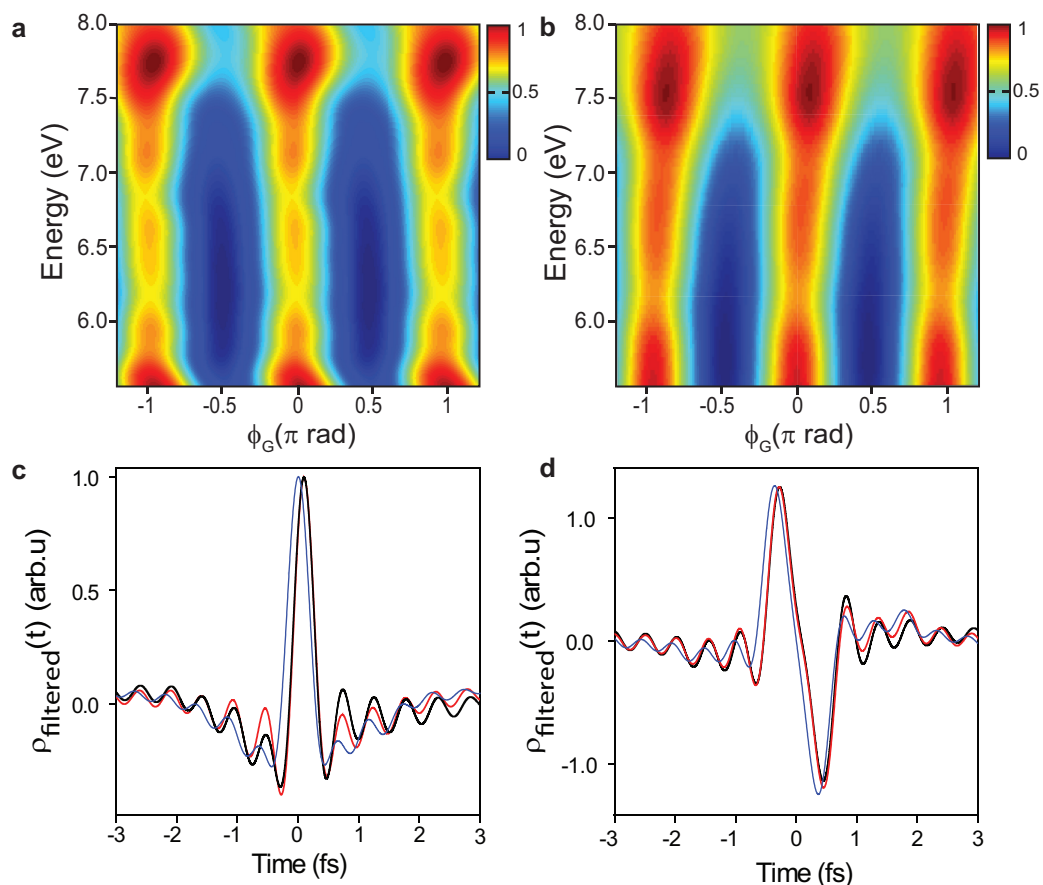


Extended Data Figure 6 | Representation of the possible multiphoton transitions on a Kr atom energy level diagram assuming third- and fifth-order nonlinear processes.



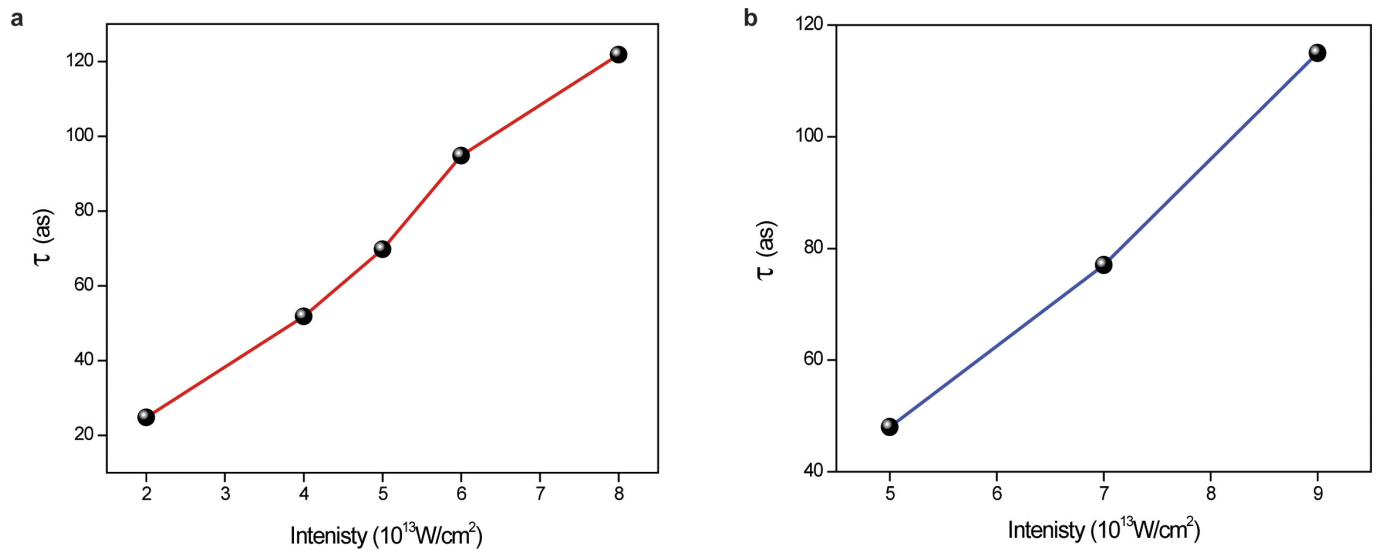
Extended Data Figure 7 | Synthetic global-phase spectrograms and nonlinear dipole fittings. a–c, Synthetic global-phase (ϕ_G) spectrograms determined using the simple model (equation (1)) with the same set of parameters (a , b , c) and delays $dt=0$ as (a), $dt=20$ as (b) and $dt=30$ as (c).

The colour scale represents spectral intensity in arbitrary units. d, e, Fits (red lines) of the spectrally filtered (d, 5.5–8 eV; e, 0–8 eV) nonlinear dipoles ($\rho(t)$, black lines) with $\phi_G \approx 0$ (left column) and $\phi_G \approx \pi/2$ rad (right column) using equation (1) and $6 \times 10^{13} \text{ W cm}^{-2}$.



Extended Data Figure 8 | Reconstruction of the global-phase spectrogram calculated by the TDSE model. **a**, Calculated spectrogram at different global-phase settings ($\phi_G = -1.2\pi - 1.2\pi$ rad) of the optical attosecond pulse using the TDSE model. **b**, Reconstructed spectrogram using the model of equation (1). The colour bar represents spectral

intensity in arbitrary units. **c**, **d**, Calculated nonlinear dipoles using the TDSE model at $\phi_G \approx 0$ (**c**) and $\phi_G \approx \pi/2$ rad (**d**) are plotted in black; the reconstructed nonlinear dipoles and the adiabatic dipoles are shown in red and blue, respectively.



Extended Data Figure 9 | Intensity dependence of the nonlinear dipole delay. a, b, The delay between the adiabatic dipole and the calculated dipole using the TDSE model as a function of the peak intensity according to TDSE simulations (a) and evaluated from the experimental data (b; see Fig. 4).

Extended Data Table 1 | Ionization and excitation probabilities calculated using TDSE simulations of Kr for a range of peak intensities of the optical attosecond pulse

Peak intensity (10^{13} W/cm ²)	1	2	4	6	8	10
Ionization probability (%)	0.0018	0.06	0.18	0.84	1.38	2.4
Excitation probability (10^{-4} %)	0.004	0.05	0.825	1.88	3.63	3.8